

Vertical Bifacial Solar Farms: Physics, Design, and Global Optimization

M. Ryyan Khan^{b,1}, Amir Hanna^{a,1}, Xingshu Sun^{b,1}, Muhammad A. Alam^{b,1,*}

^aElectrical Engineering Department, King Abdullah University of Science and Technology, Saudi Arabia

^bSchool of Electrical and Computer Engineering, Purdue University, West Lafayette, IN 47906, United States

Abstract

There have been sustained interest in bifacial solar cell technology since 1980s, with prospects of 30-50% increase in the output power from a stand-alone single panel. Moreover, a vertical bifacial panel reduces dust accumulation and provides two output peaks during the day, with the second peak aligned to the peak electricity demand. Recent commercialization and anticipated growth of bifacial panel market have encouraged a closer scrutiny of the integrated power-output and economic viability of bifacial solar farms, where mutual shading will erode some of the anticipated energy gain associated with an isolated, single panel. Towards that goal, in this paper we focus on geography-specific optimizations of *ground-mounted vertical bifacial solar farms for the entire world*. For local irradiance, we combine the measured meteorological data with the clear-sky model. In addition, we consider the detailed effects of direct, diffuse, and albedo light. We assume the panel is configured into sub-strings with bypass-diodes. Based on calculated light collection and panel output, we analyze the optimum farm design for maximum yearly output at any given location in the world. Our results predict that, regardless of the geographical location, a vertical bifacial farm will yield 10-20% more energy than a traditional monofacial farm for a practical row-spacing of 2m (1.2m high panels). With the prospect of additional 5-20% energy gain from reduced soiling and tilt optimization, bifacial solar farm do offer a viable technology option for large-scale solar energy generation.

Keywords: Bifacial solar cell, vertical panel, solar farm, global output.

1. Introduction

A conventional monofacial panel collects light only from the front side; the opaque back-sheet prevents collection of light scattered from ground (or surroundings) onto the back face of these panels. This extra energy from albedo can be partially recovered using a bifacial panel, where both faces of the panel and the cells are optically transparent. The concept of bifacial panels have been analyzed and experimentally demonstrated since 1980s [1, 2]. Indeed, an isolated bifacial panel has been shown to have up to 50% extra output [2] compared to a monofacial panel. Moreover, recent improvements in the design and fabrication of bifacial cell technology suggest several additional advantages [3]. For example, bifacial cells have a lower operating temperature (absence of infrared absorption at back metal) and better temperature coefficient (e.g., HIT cells)—which would improve lifetime and integrated power output.

Several studies in the literature have reported energy output of isolated, *standalone* bifacial panels both numerically [4, 5, 6, 7] and experimentally [8, 9, 10]. These studies include optimization of the tilt angle and elevation from ground for a single bifacial panel at various locations in

the world. The recent work by Guo *et al.* [11] provides a global analysis of vertical bifacial panel. Given an albedo threshold, they have shown that an isolated vertical panel will always produce more power compared to an optimally tilted monofacial panel, irrespective of the geographic location.

The energy gain of an isolated panel defines the upper limit of the performance potential of a solar cell technology. Eventually, the panels will have to be installed in a farm, where one must account for the mutual shading of the panels. Clearly, the area-averaged power output will now be reduced. Under these circumstances, it is not clear if the advantages found for isolated panels can still sustain. Recently, Appelbaum [12] has provided a partial answer by analyzing a solar farm at Tel-Aviv (latitude 32°N). His work focused on vertically vs. optimally tilted bifacial panel arrays. The optimally tilted farm yields 32% more energy than the vertical farm (in latitude 32°N)—however, it is not clear how the outputs compare to the monofacial panel array. It is also difficult to know if the conclusions apply to other regions of the world. An analysis that broadens the previous work to all the locations of the world (a global optimization) will be helpful. This analysis is particularly important because ITRPV roadmap projects that the bifacial market share will increase from 5% in 2016 to 30% in 2026 [13]. Many PV manufacturers (e.g., Panasonic, Prism Solar, LG, SolarWorld, Centrotherm, etc.)

*Corresponding author

Email address: alam@purdue.edu (Muhammad A. Alam)

¹The authors contributed equally.

are now producing bifacial panels. A few recent solar farms (e.g., Asahikawa Hokuto Solar Power Plant in Japan, and La Silla PV plant in Chile) are utilizing bifacial panels. Given this rapid progress, it is important to clearly understand the complex physics, design, and optimization of bifacial solar farms.

Among various farm configurations, vertically aligned bifacial panels have been of particular interest because of reduced soiling (dirt or snow) which increases overall energy output. In addition, the higher output in the afternoon due to the ‘double-humped’ daily output profile [11] coincide with the peak electricity demand. Since optimally tilted bifacial panels will always produce slightly more energy compared to the vertical farms, the analysis of vertically aligned panels may be viewed as a lower limit of energy produced by an optimized bifacial farm.

In this paper, we offer detailed model, physics, and a worldwide perspective regarding ground-mounted vertical bifacial solar farms.

We combine the global meteorological data from NASA with the clear-sky model from Sandia to estimate hourly insolation. This new algorithm bypasses the loading of extremely large hourly database, and allows efficient computation towards global analysis of new technologies while maintaining realistic and daily averaged meteorological information.

Next, we model the direct and diffused light collection [14, 15, 16], as well as the non-trivial physics of albedo light collection [17, 7] while accounting for relevant shadings on the panels and the ground. Our generalized formulation models the non-uniform illumination along the panel height. Only a fraction of the light incident on the panels will produce electricity [18] because of the spatially non-uniform illumination and the nature of the electrical connection for the panels. The second aspect is often not accounted for in literature. We use the spatially non-uniform light collection data along with the appropriate circuit model of the panels to accurately find the hourly *energy-output* from the panels and the farm.

Mutual shading between adjacent panels penalizes energy-output, thereby restricting panels from being closely packed in the farm. We explain how this results in an optimum period between the panels. At high latitudes, the sun-path is more tilted, resulting in larger optimum panel-period. In addition, at the same latitude, locations with more diffuse insolation tend to have a larger panel-period.

Finally, we present a global perspective on the annual yield of vertical bifacial solar farms. The key conclusion of the paper is this: With inter-row separation of 2m (typically required for maintenance) for 1.2m wide panels, a ground-mounted vertical bifacial farm outperforms a traditional monofacial farm by 10-20%, regardless of the geographical location. The gain may persist even for smaller inter-row separation, once the energy loss due to soiling [19, 20, 21, 22] is accounted for. The performance gain requires a denser packing of vertical bifacial panels, the

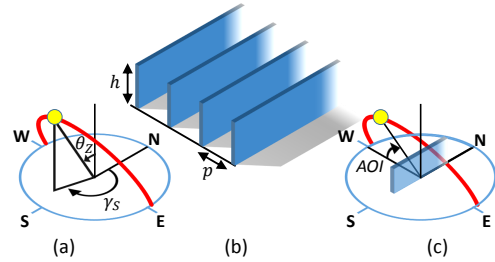


Figure 1: (a) The zenith and azimuth angles (θ_Z , γ_S) of the sun is shown at a specific time. An example of the sun-path is shown by the red line. (b) The vertical bifacial solar farm is depicted with relevant definitions. (c) This shows the angle of incidence (AOI) on the panel at the specific solar position.

implication of which must be accounted for in the levelized cost of electricity (LCOE) calculation [23, 24].

In sections 2.1 and 2.2, we present the details of the irradiance model, and the physical model to calculate the light collection and power generation of the panels and the farm. In sections 3.1-3.3, we discuss the physics and design-optimization of the farm. Finally, in section 3.4, we present the global perspective and prospects of the optimally designed vertical bifacial solar farm. Our conclusions are summarized in section 4.

2. Method

2.1. Irradiance model

2.1.1 Simulation of hourly GHI. Temporal solar irradiance data consist of the position of the sun and its intensity. This information is crucial to simulate and optimize the energy yield of solar farms.

To simulate such data, we first start by calculating the position of the sun (solar Zenith θ_Z and Azimuth γ_S angles) at arbitrary time and geographic locations by using the NREL’s solar position algorithm [25] implemented in Sandia model library [26]. Here, θ_Z is the refraction-corrected Zenith angle, which depends on altitude and ambient temperature. Second, we input the sun position data into the Haurwitz clear sky model to generate the Global Horizontal Irradiance (GHI or I_{GHI}) [27, 28] on a minute-to-minute basis. Note that the clear sky model often overestimates insolation, especially when the atmosphere is cloudy or overcast. Hence, in the third and final step, we integrate the simulated GHI over time, which is then scaled to match the satellite-derived monthly average GHI data (for 22 years) from the NASA Surface meteorology and Solar Energy database [29], whereby local variation of GHI caused by cloudiness and altitude is incorporated into the calculation. Therefore, our modeling framework fully incorporates the impacts of geographic and climatic factors into modeling the solar irradiance.

2.1.2 Decomposition of GHI into DHI and DNI.

Calculating the irradiance on a tilted surface requires decomposing GHI into two components: Direct Normal Irradiance (DNI or I_b) and Diffuse Horizontal Irradiance (DHI or I_{diff}). The relationship between the two components can be written as

$$I_{GHI} = I_b \cos \theta_Z + I_{diff}. \quad (1)$$

Based on (1), however, it is impossible to separate I_b and I_{diff} from I_{GHI} . Therefore, we estimate the diffuse fraction of I_{GHI} using the Orgill and Hollands model which empirically calculate the diffuse fraction using the clearness index of the sky (k_T) [30]. The clearness index is defined as the ratio between I_{GHI} and extraterrestrial irradiance (I_0) on a horizontal surface, i.e.,

$$k_T = \frac{I_{GHI}}{I_0 \times \cos \theta_Z}. \quad (2)$$

For a specific time and location, I_{GHI} is already known while the extraterrestrial irradiance can be evaluated analytically [31]; therefore, we can obtain the clearness index k_T on a minute-to-minute basis using (2). Knowing I_{GHI} and k_T , we use the Orgill and Hollands model to determine I_{diff} , which allows us to deduce I_b from (1). For demonstration, an example calculation of irradiance at Washington DC on September 22 is shown in Fig. 2.

There are several empirical models for decomposing GHI found in literature [32, 33, 34]. Generally, good agreement have been found among these models [35]. Also, we assume isotropic sky model [36] for diffuse irradiance I_{diff} . The Perez model [37] provide a more elaborate and somewhat more complex representation of the diffuse light. However, we expect that our numerical results and key conclusion will not be overly sensitive to the model chosen, and the general conclusions will hold irrespective of the assumed models.

2.1.3 Angle of Incidence (AOI) calculation. To evaluate the contribution of the beam component of sunlight (i.e., I_b), we need to calculate the angle of incidence (AOI) between I_b and the front/back surface of vertical bifacial solar panels. It turns out that AOI of an east-west facing vertical bifacial solar panel can be simply expressed as

$$\theta^{(F)} = AOI_{front} = \cos^{-1} [\sin \theta_Z \times \cos(\gamma_S - \pi/2)], \quad (3)$$

$$\theta^{(B)} = AOI_{back} = \cos^{-1} [\sin \theta_Z \times \cos(\gamma_S + \pi/2)]. \quad (4)$$

for the front and back surfaces, respectively. In the next section, knowing the angular and irradiance data of sunlight, we will show how to evaluate the optical absorption and power generation of vertically-mounted bifacial solar farms.

2.2. An array collects direct, diffuse, and albedo light

The solar farm consists of vertical bifacial panels of height h , separated by a period of p , as shown in Fig.

1(b). Each of the panels face E-W and run infinitely along N-S direction. The front face (East facing) sees the sun from sunrise until noon. The back face (West facing) of the panel sees the sun from noon until sunset. In the following, we will first explain light collection by individual panels and we will integrate the contributions from the array to calculate total power output from the farm.

2.2.1 Panel properties: uniform illumination. Let us assume the panels have monofacial-efficiency of η for uniform, normal illumination onto the panel. For an angle of incidence (AOI) θ , we can approximate the efficiency as $\eta(\theta) \equiv [1 - R(\theta)] \times \eta$. The angle dependent reflectivity of the panel can be empirically written as [38]

$$R(\theta) = 1 - \frac{1 - \exp(-\cos \theta/a_r)}{1 - \exp(-1/a_r)}. \quad (5)$$

Here, a_r is the angular loss coefficient. In the following calculations, we assume $a_r = 0.16$, typical for commercial Si solar panels [38].

The efficiency η_{diff} of the panel under diffuse sunlight (isotropic illumination) will be lower than that under normal (direct) illumination. We assume $\eta = 18.9\%$ and $\eta_{diff} = 15.67\%$ under normal and diffuse illumination on a single face of the panel (estimated using the simulator ‘Tracey’ [39, 40, 41]: see Supplementary Information (SI)). Oblique angles in the diffuse light have higher reflection loss than normal incidence—that is why $\eta_{diff} < \eta$.

Experimentally, the cell efficiency observed by illuminating front or the back faces differ by 1-2% [3]. For simplicity, we assume these values to be the same. Our formulation is general, and can be applied for the bifacial efficiency asymmetry by using separate values of $\eta^{(F)}$ and $\eta^{(B)}$ for front and back face efficiencies, respectively.

At any specific time of the day, the two faces of a bifacial panel are illuminated asymmetrically. Therefore, we calculate the power collection from the front and back faces separately. Let us assume that at any given time of the day, AOI for the front and back panel faces are $\theta^{(F)}$ and $\theta^{(B)}$, respectively. We will focus on the power collection from the front face, and the calculations for the back face will follow a similar approach. We will denote power per unit area of the *panel-surface* and per unit area of the *farm-land* by $\hat{I}_{PV(*)}$ and $I_{PV(*)}$, respectively.

2.2.2 Panel properties: non-uniform illumination.

During mornings and afternoons, mutual shadowing makes the illumination over the panel spatially non-uniform, with the lower part of the panel receiving less light than the top. For a panel constructed from a set of series connected cells, bypass diodes are placed across different sub-sections of the series-string to avoid reverse breakdown of the shaded cells. We assume $N_{bypass} = 3$ bypass diodes sub-divide each panel into $N_{bypass} = 3$ strings. The effect of the shading on lowering the panel output is taken into

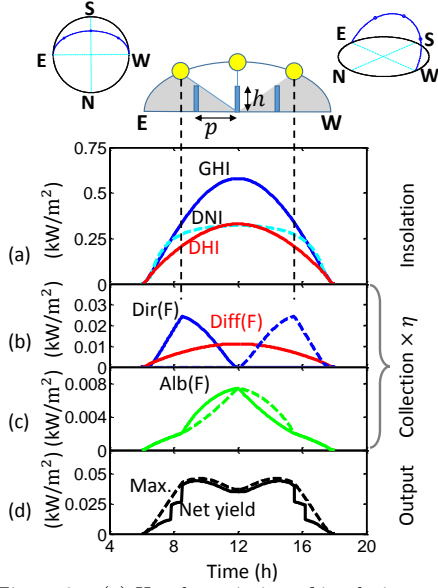


Figure 2: (a) Hourly variation of insolation components for Washington DC on September 22. (b, c, d) The power generation components of the farm is shown. Here, we have assumed $h = 1.2\text{m}$ and $p = 2\text{m}$.

account based on the analytical approach developed by C. Deline *et al.* [42]. In this calculation, we assume that the total current is always limited by the bottom string; the validity of the assumption is discussed in the SI-document.

2.2.3 Direct insolation collection. At any given time of the day, direct illumination component normal to the panel is $I_b \cos \theta^{(F)}$ for the unshaded part of the panel (i.e., $z > h_s$), see Fig. 6(c). Here, z is any position along the height on the panel, and h_s is the shadow on the panel [14, 15] the corresponding time of the day. Considering the reflection loss $R(\theta^{(F)})$ and the panel efficiency $\eta^{(F)}$, we find the power generated per surface area at height z of the front face of the panel as follows,

$$\hat{I}_{PV(dir)}^{(F)}(z) = \begin{cases} [1 - R(\theta^{(F)})]\eta^{(F)} I_b \cos \theta^{(F)}, & z > h_s \\ 0, & z \leq h_s. \end{cases} \quad (6)$$

Here, $\hat{I}_{PV(dir)}^{(F)}(z)$ is the power generation component only from the direct/beam sunlight. The corresponding integrated ‘maximum’ power (*per unit farm area*) from the direct sunlight is given by:

$$\begin{aligned} I_{PV(dir),0}^{(F)} &= \frac{1}{p} \times \int_0^h \hat{I}_{PV(dir)}^{(F)}(z) dz \\ &= \frac{(h - h_s)}{p} [1 - R(\theta^{(F)})]\eta^{(F)} I_b \cos \theta^{(F)}. \end{aligned} \quad (7)$$

We quote $I_{PV(dir),0}^{(F)}$ as the ‘maximum’ output from direct light as this does not assume any loss due to non-uniform generation in the series connected string of cells. This maximum may be reached, for example, in a thin-film

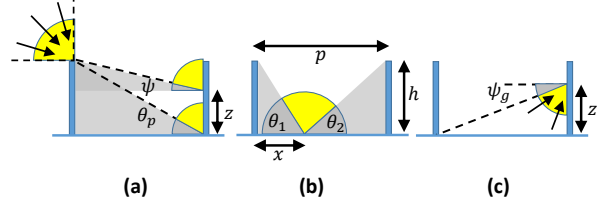


Figure 3: (a) Partial masking of DHI on a face of the panel. (b) Partial masking of DHI on the ground. The fractional DHI reaching the ground is a source for albedo light. (c) Collection of the above mentioned albedo light.

like panel configuration. The solid line in Fig. 2(b) shows $I_{PV(dir),0}^{(F)}$ as the day progresses. After the solar-noon, the front face will not directly see the sun, therefore $I_{PV(dir),0}^{(F)} = 0$ for the later part of the day. Similarly, the back face shows a mirrored characteristic for $I_{PV(dir),0}^{(B)}$ as shown by the dashed line. These two components together contribute to the characteristic double-humped hourly output profile of a vertical bifacial panel.

2.2.4 Diffuse insolation collection. Ideally, when the panels are far apart, half of the diffuse rays angle towards the front-face of the panel. These rays cover zenith angle range of $[-\pi/2, 0]$. However, a fraction of these angles is obstructed/shaded when the panels are arranged in an array—depicted by the shaded quarter circles in Fig. 3(a). In this illustration, we see that the top portion of the vertical panel receives more diffuse light than the bottom. Calculation of diffuse insolation collection using the well-known average diffuse masking angle [14] will yield in an overestimated value, especially for highly tilted panels. An appropriate view factor [12] properly estimates the diffuse light collection.

The incident diffuse light intensity at height z of the panel (see Fig. 3(a)) is $I_{diff} \times F_{dz-sky}$. The diffuse light is masked at angle $\psi(z)$ resulting in the view-factor (towards the unobstructed sky) of $F_{dz-sky} = (1 - \sin \psi(z))/2$ at z [43]. The corresponding power generation per panel area (front face) from the diffuse insolation is as follows,

$$\begin{aligned} \hat{I}_{PV(diff)}^{(F)}(z) &= \eta_{diff}^{(F)} [I_{diff} \times F_{dz-sky}] \\ &= \eta_{diff}^{(F)} \left[I_{diff} \times \frac{1}{2}(1 - \sin \psi(z)) \right]. \end{aligned} \quad (8)$$

And, the corresponding integrated, ‘maximum’ power generation *per unit farm area* from the diffuse light is:

$$\begin{aligned} I_{PV(diff),0}^{(F)} &= \frac{1}{p} \times \int_0^h \hat{I}_{PV(diff)}^{(F)}(z) dz \\ &= \frac{h}{p} \eta_{diff}^{(F)} \left[I_{diff} \times \frac{1}{2}(1 - \tan(\theta_p/2)) \right]. \end{aligned} \quad (9)$$

Here, $\theta_p = \tan^{-1}(h/p)$. The hourly variation of $I_{PV(diff),0}^{(F)}$ is shown by the red solid line in Fig. 2(b). As expected,

this component of power generation peaks at noon when the DHI (I_{diff}) also peaks. In the above calculations, we can find $\hat{I}_{PV(diff)}^{(B)}(z)$ and $I_{PV(diff),0}^{(B)}$ for the back face by replacing $\eta_{diff}^{(F)}$ with $\eta_{diff}^{(B)}$.

2.2.5 Albedo light collection. Let us first describe the effect of diffuse insolation on albedo. As explained in the preceding discussion, there is a fractional-shadowing (or masking) of the diffuse light reaching the panel. A similar scenario is true for diffuse light reaching the ground. And, depending on the position between the panels, the amount of diffuse sunlight reaching the ground is different.

Consider a position x between adjacent panels, as in Fig. 3(c). The masking angles from the two panels are:

$$\theta_1(x) = \tan^{-1} \frac{h}{x} \quad \text{and} \quad \theta_2(x) = \tan^{-1} \frac{h}{p-x}. \quad (10)$$

The average masking angles can be written as,

$$\bar{\theta}_1 = \frac{1}{p} \int_0^p \theta_1(x) dx = \theta_p + \frac{\ln(\csc \theta_p)}{\cot \theta_p}. \quad (11)$$

Due to symmetry: $\bar{\theta}_1 = \bar{\theta}_2$. Here, $\theta_p = \tan^{-1}(h/p)$. The average diffuse insolation reaching the ground is,

$$I_{Gnd:diff} = I_{diff} \times \frac{1}{2} (\cos \bar{\theta}_1 + \cos \bar{\theta}_2) = I_{diff} \times \cos \bar{\theta}_1. \quad (12)$$

Note that $\bar{\theta}_1$ is constant throughout the day, and $I_{Gnd:diff}$ is proportional to I_{diff} . Diffuse masking on the ground has not been considered in prior literature, although the contribution is particularly important for typical p/h . For example, with $p/h \sim 1$, the DHI I_{diff} may be masked more than 50% (i.e., $\cos \bar{\theta}_1 < 0.5$). Now, $I_{Gnd:diff} \times R_A$ can be the diffused light source for the front (or back) face of the panel. The albedo light collection originating from diffuse insolation is masked at angle $\psi_g(z)$ at height z on the panel, see Fig. 3(c). Therefore, the corresponding power generation per panel front surface at z is:

$$\begin{aligned} \hat{I}_{PV(Alb:diff)}^{(F)}(z) &= \eta_{diff}^{(F)} I_{Gnd:diff} R_A \times F_{dz-gnd} \\ &= \eta_{diff}^{(F)} I_{Gnd:diff} R_A \times \frac{1}{2} (1 - \sin \psi_g(z)). \end{aligned} \quad (13)$$

The corresponding integrated, ‘maximum’ power generation *per unit area* is given by:

$$\begin{aligned} I_{PV(Alb:diff),0}^{(F)} &= \frac{1}{p} \int_0^h \hat{I}_{PV(Alb:diff)}^{(F)}(z) dz \\ &= \frac{h}{p} \eta_{diff}^{(F)} I_{Gnd:diff} R_A \times \frac{1}{2} (1 - \tan(\theta_p/2)). \end{aligned} \quad (14)$$

Next, we can consider albedo from the direct insolation [17]. In the morning, the shading on the ground will be configured as shown in Fig. 4(a). The shade length s_1

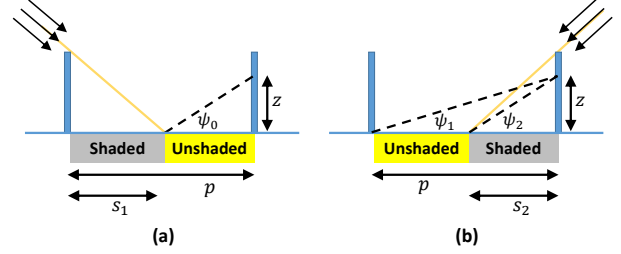


Figure 4: Partial shading of the ground due to DNI during (a) morning, and (b) afternoon.

is equal to the period p (i.e., ground fully shaded for the beam component) when the array is turned on. The shade goes away ($s_1 = 0$) at noon. At any time of the day, the unshaded length ($p - s_1$) subtends angles $[\psi_0, \pi/2]$ at the point z on the front panel face (see Fig. 4(a)). In the afternoon, shading s_2 is adjacent to the front face, Fig. 4(b). In this case, the unshaded region subtends angles $[\psi_1, \psi_2]$ at the point z on the front panel face. We can write:

$$\begin{aligned} \psi_0(z) &= \cot^{-1} \left(\frac{p - s_1}{z} \right), \\ \psi_1(z) &= \cot^{-1} \left(\frac{p}{z} \right) \quad \text{and} \quad \psi_2(z) = \cot^{-1} \left(\frac{s_2}{z} \right). \end{aligned} \quad (15)$$

The shadow length s_1 (or s_2) is calculated for each time-step of the day [14, 15]. Finally, the power generated per area of panel front-face at z from albedo originating from the direct sunlight is calculated as follows:

$$\hat{I}_{PV(Alb:dir)}^{(F)}(z) = \eta_{diff}^{(F)} I_{dir} R_A \times F_{dz-Ugnd}, \quad (16)$$

where, the view factor from the position z on panel-face to the unshaded part of the ground is given by,

$$F_{dz-Ugnd} = \begin{cases} \frac{1}{2} (1 - \sin \psi_0(z)), & \text{(before noon)} \\ \frac{1}{2} (\sin \psi_2(z) - \sin \psi_1(z)), & \text{(afternoon)}. \end{cases} \quad (17)$$

And, the corresponding integrated, ‘maximum’ power generated *per farm area* is:

$$\begin{aligned} I_{PV(Alb:dir),0}^{(F)} &= \frac{1}{p} \int_0^h \hat{I}_{PV(Alb:dir)}^{(F)}(z) dz \\ &= \frac{h}{p} \eta_{diff}^{(F)} I_{dir} R_A \times F_{PV-Ugnd}, \end{aligned} \quad (18)$$

where, the view factor from the full panel-face to the unshaded part of the ground is given by,

$$F_{PV-Ugnd} = \begin{cases} \frac{1}{2} \left(1 - \tan \frac{\psi_0(h)}{2} \right), & \text{(before noon)} \\ \frac{1}{2} \left(\tan \frac{\psi_2(h)}{2} - \tan \frac{\theta_p}{2} \right), & \text{(afternoon)}. \end{cases} \quad (19)$$

The net ‘maximum’ albedo light contribution from the front-face ($I_{PV(Alb),0}^{(F)} = I_{PV(Alb:dir),0}^{(F)} + I_{PV(Alb:diff),0}^{(F)}$) is

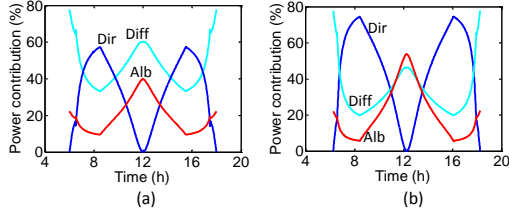


Figure 5: Fractional panel-illumination contribution of direct, diffuse, and albedo light on September 22 in (a) Washington DC, and (b) Jeddah.

shown by the solid line in Fig. 2(c). For the back-face, $I_{PV(Alb.dir),0}^{(B)}$ just the flipped version around noon.

Finally, combining Eqs. (7), (9), (14), (18), the ‘maximum’ net power generated per farm area is

$$\begin{aligned}
 I_{PV,0}^{(bifacial)} &= \left[I_{PV(dir),0}^{(F)} + I_{PV(dir),0}^{(B)} \right] + \left[I_{PV(diff),0}^{(F)} + I_{PV(diff),0}^{(B)} \right] \\
 &\quad + \left[I_{PV(Alb),0}^{(F)} + I_{PV(Alb),0}^{(B)} \right] \quad (20) \\
 &= I_{PV(dir),0}^{(bifacial)} + I_{PV(diff),0}^{(bifacial)} + I_{PV(Alb),0}^{(bifacial)} \quad (21)
 \end{aligned}$$

The black dashed line in Fig. 2(d) shows $I_{PV,0}^{(bifacial)}$ as the day progresses. Due to partial shading and non-uniform illumination, however, it is not possible to extract this power from the panel configured with the string and bypass-diode connection. A detailed calculation results in the final power generation $I_{PV}^{(bifacial)}$ per farm area, see black solid line in Fig. 2(d). The abrupt jumps correspond to times when the bypass diodes turns on or off certain sub-strings on the panel. Notice that $I_{PV}^{(bifacial)} < I_{PV,0}^{(bifacial)}$ throughout the day. The residual double-humped feature originates from the direct insolation component; otherwise, the power-generation profile is flattened by diffuse and albedo light.

3. Results and Discussion

3.1. Hourly energy output

For the following calculations, we assume a typical panel height of $h = 1.2\text{m}$ and the albedo reflectance of 0.5. Albedo reflectance of 0.5 or more is observed naturally for snow-covered ground, or can be achieved artificially for example by white concrete [44].

As discussed earlier, the hourly insolation and power generation from a farm (with period $p = 2\text{m}$, i.e., $p/h = 1.667$) is shown in Fig. 2 for Washington DC (September 22). The fractional contribution of each component (direct, diffuse, and albedo) provides additional information about how the vertical bifacial panel behaves under various weather conditions. For example, in September, the insolation in Washington DC is more diffuse compared to Jeddah. Fig. 5 show the hourly fractional generation from the three components for Washington DC and Jeddah, respectively. We observe that the fractional contribution

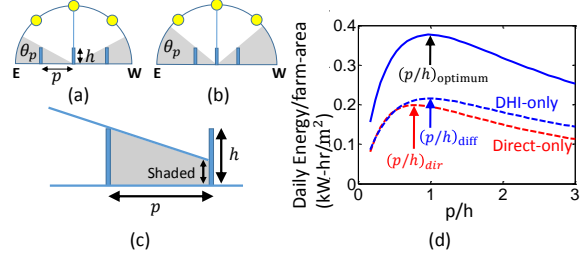


Figure 6: Low elevation of the sun in early morning and late evening causes mutual shading between adjacent panels. The shaded region in (a, b) indicates the time or solar positions when there is mutual shading. Clearly, larger panel-gap p will have shorter shading time as in (a). (c) shows partial shading of a panel for early morning. (d) A single day energy output per farm area is shown (Sept. 22) by the blue solid line. The blue and red dashed line corresponds to the cases when only diffuse sunlight (DHI-only), and only direct sunlight (Direct-only) is considered respectively.

from diffuse and albedo light peaks at noon. In Washington DC, diffuse and direct components have similar contributions in early part of the day (8-10h). On the other hand, the generation from diffuse light is much lower than direct in early (8-10h) or late (14-16h) part of the day in Jeddah—this indicates that Jeddah has a more clear sky (i.e., mainly direct light). This will affect the net power production at noon. As there is no contribution from direct light at noon, a higher fraction of diffuse light can even out the hourly output variation.

As we will see later, the output varies as a function of the p/h -ratio. Therefore, the discussions above hold for any h while $p/h = 1.667$ is maintained.

3.2. Effect of panel array period p

Next let us consider the effect of the period p on the farm output. Due to the array configuration, front-face of a panel is partially illuminated (partially shadowed) in the early part of the day. For example, in Fig. 6(c), we see the bottom part of the panel is shaded when sun’s elevation is low. In this situation, the bypass diode will turn-off the bottom string of the panel, thereby limiting the output from only the top part of the panel. Similar situation occurs for the back-face of the panel before sunset. The shadow-limited-operating conditions are shown as gray-shaded region in Fig. 6(a, b).

When the panels are packed close (i.e., small p), the panels on the farm have bypass-diode limited operation for a long period of each day—this greatly reduces power generation compared to light collection. Again, at large p , the output of each panel saturates (to “standalone” panel limit), and thus the farm output per unit area will decrease with increasing p . Therefore, there is an optimum p for which the power output *per land area* is maximized, also shown by the blue solid line in Fig. 6(d). The optimum p scales proportionally with h , i.e., universality of the design holds for the p/h ratio. The universality may be understood by realizing that all the expressions for insolation

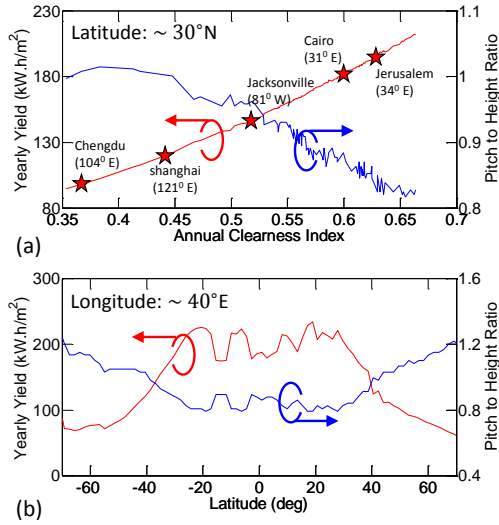


Figure 7: Annual yield and optimum p/h as function of (a) annual clearness index \bar{k}_T (latitude 30°N), and (b) latitude (at longitude 40°E).

collection contain the ratio p/h . For a farm design, instead of integrating over a single day, the output is integrated over the whole year to find a functional relation similar to the one shown in Fig. 6(d) for ‘net annual energy versus p/h ’. This allows us find maximum annual yield and the corresponding optimum p/h for that specific location. Subsequently, the analysis is repeated for various locations across the globe and a map of the location-specific optimum p/h is shown in Fig. 8(b). The worldwide optimum p/h will be discussed in the next section. It is important to highlight that energy per land area is but one metric of optimization. A levelized cost of electricity (LCOE) optimization will be a part of a future study, but we believe the key conclusion will remain the same.

3.3. Effect of clearness index and latitude.

At a given latitude on Earth, the tilt of the sun and the sun-path is the same for all longitudes. Ideally, we can thus expect the insolation to depend only on latitude. However, variation in meteorological conditions over longitudes at a set latitude causes variation in GHI, clearness index, and the fractional contribution of diffuse insolation. Such variation in weather affects the optimal design of the vertical bifacial solar farm and its yearly yield. For example, in Fig. 7(a) we present the optimum p/h (blue) and the corresponding yearly output (red line) of the farm as a function of annual clearness index \bar{k}_T at latitude 30°N—the locations corresponding to the various \bar{k}_T are also marked in the figure. Here, we optimize p/h to maximize the annual yield, and calculate the corresponding farm output for different longitudes, but at a fixed latitude 30°N. Then

the results are sorted as a function of corresponding \bar{k}_T to obtain the plots shown in Fig. 7(a).

At a set latitude, the sun-path is fixed (for all longitude), which in turn determines the panel shadow length and dominates the choice of optimum p/h . However, as shown in Fig. 7(a), at a fixed latitude 30°N, there is a small variation in optimum p/h with \bar{k}_T . In order to understand why p/h decreases with \bar{k}_T , we need to explain the relative roles of diffuse and direct light. In Fig. 6(d), the blue and red dashed lines consider solar sources when only the diffuse and direct light are present, respectively. For the ‘Direct-only’ case (red dashed line), the diffused light contribution is set to zero and only the direct light and its corresponding albedo contributions are used to calculate the energy output. The output is maximized at $(p/h)_{dir}$, as marked by the red arrow. Similarly, for the ‘DHI-only’ case (blue dashed line), the direct sunlight is set to zero, and the diffused light and its albedo contributions are accounted for. The ‘DHI-only’ contribution maximizes at $(p/h)_{diff}$, as marked by the blue arrow. In general, for any location, we find that $(p/h)_{dir} < (p/h)_{diff}$. Therefore, when \bar{k}_T is low, DHI or diffuse component dominates and the overall optimum p/h converges to $(p/h)_{diff}$. For example, note that the overall peak $(p/h)_{optimum}$ (on the blue solid line in Fig. 6(d)) is close to $(p/h)_{diff}$ position. Therefore, as shown in Fig. 7(a), reducing \bar{k}_T below 0.45 will only keep the p/h at a constant value, close to $(p/h)_{diff}$, dictated by the diffuse light component. In contrast, as \bar{k}_T increases, the direct light starts to dictate the farm output, and the optimum p/h decreases from $(p/h)_{diff}$ and shifts towards $(p/h)_{dir}$. Obviously, by definition, increasing \bar{k}_T increasing GHI. Therefore, the optimum yearly yield increases with \bar{k}_T .

The locations with higher latitudes sees larger tilt in the sun-path, and lower GHI. Therefore, the yearly output is high close to the equator and decreases at higher latitudes, as shown by red line in Fig. 7(b). From equator up to latitude $\sim 30^\circ$, the optimum p/h remains close to 0.8 (blue line), and then it increases. For higher latitudes, the tilt of the sun (i.e., θ_Z) is larger. The longer shadows results in higher spacing between the panels.

3.4. Global Map of Energy Yield

We are now ready to summarize the global optimization and energy yield of vertical bifacial solar farms. We assume a constant ground reflectance of 0.5. As explained earlier, we expect decrease in GHI and output for increasing latitudes. And, there are variation in design and output along the longitudes due to meteorological variations. The global yearly yield and the corresponding optimum p/h is shown in Fig. 8. We observe higher output in Africa and Saudi Arabia compared to India and China due to clearer sky (i.e., higher \bar{k}_T) and higher GHI. Also, optimum $p/h \sim 0.8$ is close to equator, and begins to increase above 30° latitude. *The optimum p/h is within 0.8-1 for most of the locations in the world.*

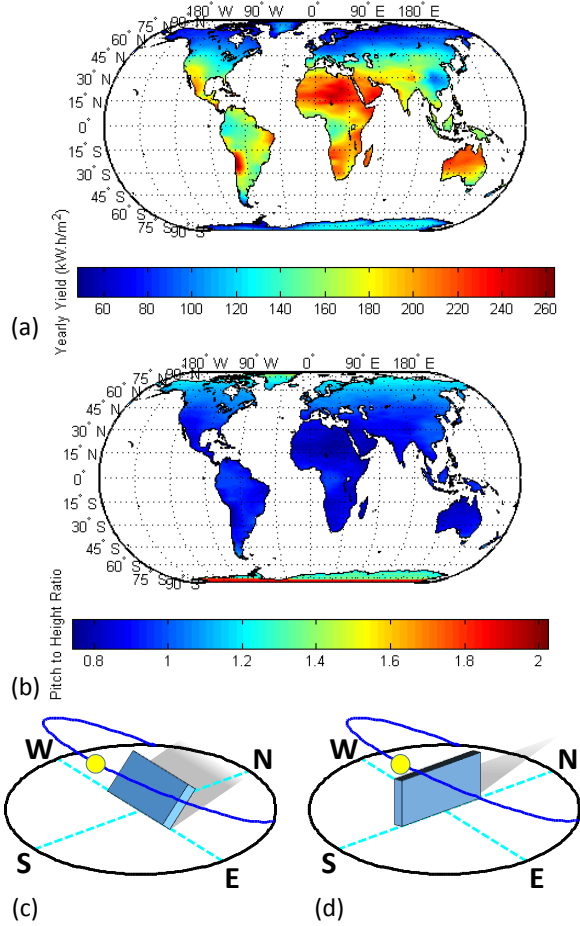


Figure 8: Global optimized (a) yearly yield, and (b) optimum p/h for the vertical bifacial farm. We have chosen constant 50% albedo reflection. The sun-path is shown for latitude 70°N (July) in (c) with South facing monofacial and (d) with East-West facing vertical bifacial panel.

We also compare the vertical bifacial solar farm with the optimized monofacial (optimized tilt [45] and spacing) solar farm. Conventionally, in a monofacial solar farm, the row spacing is selected such that the annual shading loss is less than 5%. This results in a set-back-ratio of 2 closer to equator, and 3 for mid latitudes [45]. For the monofacial farms, we take into account the direct and diffuse insolation, and neglect the albedo. We will compare two cases: when the spacing is optimized for maximum energy yield vs. when the spacing is fixed by practical considerations. Note that the comparison is somewhat biased because while the monofacial farm is tilt-optimized, the vertical farm – by definition – is not.

3.4.1 Spacing optimized solar farms. For the first comparison, we determine the optimum row spacing to maximize the area-normalized annual energy yield of monofacial and bifacial farms for a given location in the world. The ratio of the ‘maximized’ annual yield of the

vertical bifacial farm to the monofacial farm is plotted in Fig. 9(a). Close to equator, the monofacial panels are optimally tilted parallel to the ground, and the optimal row spacing is close to zero. Close to equator, therefore, monofacial panels collect the GHI fully, yielding the maximum output for *any* farm configuration. In these locations, in absence of any soiling considerations, this energy output is twice as large compared to a vertical bifacial farm. The advantage of monofacial farms decreases at higher latitude. At latitudes $> 60^\circ$, the sun-path is highly tilted. For example, consider the sun-path shown in Fig. 8(c,d) for latitude 70°N in July. The sun is at North-East (or North-West) in early (or late) part of the day. At these times, the South-facing monofacial panel does not receive any direct sunlight (Fig. 8(c)), unlike East-West facing bifacial panel (Fig. 8(d)). Moreover, closer to noon, when the insolation is more significant, we would observe a long shadow towards the North. This result in prominent shading on adjacent South-facing monofacial panels, see Fig. 8(c). The shadows towards the East or West are relatively shorter; therefore, the East-West facing vertical bifacial panels incur lower shading loss. The bifacial panels allows the vertical farm to collect more energy both from the sky and the ground compared to the optimally (and highly) tilted monofacial panel array. In these locations at high latitudes, the bifacial farm produces significantly more energy than monofacial farms.

3.4.2 Spacing with practical considerations. Recall that the period p of an array is defined by the sum of the row spacing and the horizontal distance covered by a tilted panel. Unfortunately, close to equator (within 30° latitudes), yield-optimized monofacial farms have a row-spacing less than 0.25m, which is impractically small for installation and maintenance purposes. For example, the row-spacing in the farm is required to be 2m or higher [46]. Therefore, the ‘yield-optimized’ comparison of the farms close to equator (as discussed in the preceding section) may not be practical. Therefore, next we compare the energy yield of the farms with fixed 2m row-spacing.

The ratio of the annual yield of the vertical bifacial farm to the monofacial farm, assuming 2m row-spacing for all, is shown in Fig. 9(b). The conclusion is obvious: For almost all regions of the world, ground-mounted vertical bifacial farms outperform tilt-optimized monofacial farms by 10-20%. Indeed, some regions in Africa and South America may offer 50% more energy output. However, there are a few isolated locations in the world (e.g., parts of China, Columbia, Ecuador, etc.–marked in deep blue in Fig. 9(b)) where bifacial cell under-performs a monofacial cell by 10-20%. These regions are characterized by low clearness index, so that the shading of the diffuse light at the bottom of the panel and the current-constraint associated with the lower bypass diode strongly penalizes the power output of a bifacial farm (see the corresponding regions in Fig. 8(a)). In these regions, bifacial farms may only be viable if the panels are optimized for tilt angle and energy-penalty due to soiling are accounted for. Indeed,

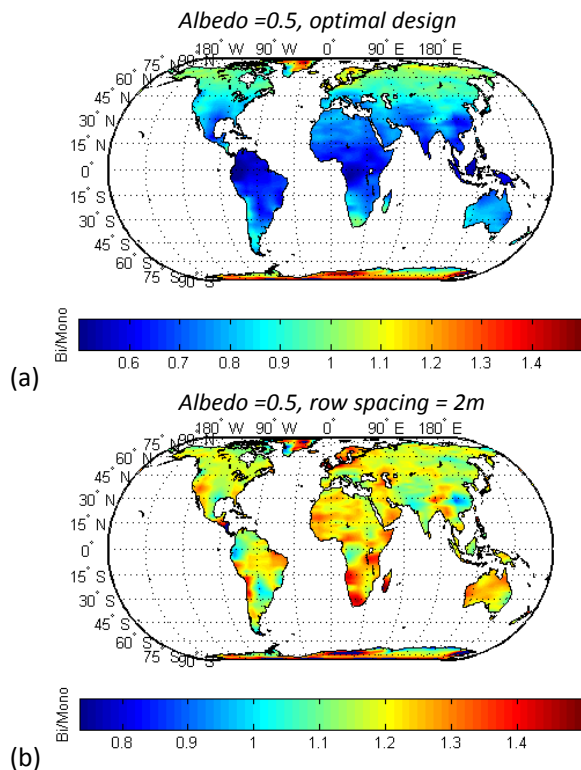


Figure 9: Ratio of yearly yield from the vertical bifacial farm to monofacial farm for (a) optimal design, and (b) fixed row spacing of 2m (1.2m wide panels). In (a), the monofacial farm has optimum panel tilt and row spacing at each location.

vertical farms seem even more attractive as cleaning costs (e.g., water, labor), etc. are expected to be lower and overall reduction in temperature will improve farm operating lifetime. Therefore, a LCOE-based optimization is essential to accurately quantify the possible gain in utilizing the vertical bifacial farm.

4. Summary and Conclusions

In this paper, we have utilized worldwide meteorological data and a detailed physical panel-array model to estimate annual yield of vertical bifacial solar farms. To summarize:

1. We have combined the daily average meteorological NASA data [29] with a *clear-sky model* from Sandia [26, 27, 28] to obtain hourly insolation information. This combined model greatly reduces loading of large database and speeds up computation while maintaining average meteorological insolation information.
2. Our physics model for panel array combines the effect of direct, diffuse, and albedo illumination onto the panels. The mutual shading and collection from direct and diffuse insolation has been modeled based on previous literature. We have discussed partial shading and illumination onto the ground between panels

due to direct and diffuse sunlight. The non-trivial collection of this albedo light has been explained in details. The spatially non-uniform illumination along the panel height can affect the final panel output—our general formulation of the model allows us to calculate such details.

3. Due to non-uniform illumination, and string of series-connected cell configured on a panel, the energy output is not proportional to the insolation collection. We assume that the panel is divided into 3 sub-strings each connected with its own bypass-diodes. The final output of the panels are calculated for this specific configuration.
4. Mutual shading between adjacent panels restricts panels being closely packed in the farm. We explain how this results in an optimum period between the panels. At high latitudes, the sun-path is more tilted, resulting in larger optimum panel-period. And, at the same latitude, locations with more diffuse insolation (i.e., lower k_T) tend to have a larger panel-period.
5. We present a global perspective on the annual yield of vertical bifacial solar farms. For a practical row-spacing of 2m, the energy yield of bifacial solar farms continues to outperform the monofacial solar cells in most of the regions of the world, although the energy gain is somewhat smaller compared to stand-alone panels [11].

Finally, we wish to highlight three factors that will impact the LCOE of a solar farm, but were deemed beyond the scope of the paper. First, the increased energy yield of a bifacial farm requires closely spaced panels. Since the bifacial panels are somewhat more expensive, the LCOE must be calculated carefully to reflect this additional cost. Second, a recent study shows that vertical panels have low dust accumulation while having energy yield similar to conventional tilted panels [47], because of the *soiling penalty* associated with the monofacial cells. Moreover, cleaning the panels is expensive. Therefore, the energy gain of vertical farms, in practice, may be higher than those summarized in Fig. 9. Finally, a farm designed with optimally tilted and *elevated* panel array produces much more energy than a ground-mounted vertical bifacial farm [12]. Overall, these energy gains must be balanced carefully with the increased installation cost to ensure the worldwide economic viability of the bifacial solar farms.

Acknowledgement

We gratefully acknowledge Dr. C. Deline from NREL who read the initial draft of the paper and highlighted the importance of bypass diodes regarding the energy yield of bifacial farms. This work was made possible through financial support from the National Science Foundation through the NCN-NEEDS program, contract 1227020-EEC and by the Semiconductor Research Corporation, the US-India

Partnership to Advance Clean Energy-Research (PACE-R) for the Solar Energy Research Institute for India and the United States (SERIUS), U.S. Department of Energy under Contract No. DE-AC36-08GO28308 with the National Renewable Energy Laboratory, the Department of Energy under DOE Cooperative Agreement No. DE-EE0004946 (PVMi Bay Area PV Consortium), and the National Science Foundation under Award EEC1454315-CAREER: Thermophotonics for Efficient Harvesting of Waste Heat as Electricity.

References

- [1] A. Luque, A. Cuevas, J. Ruiz, [Double-sided n+-p-n+ solar cell for bifacial concentration](#), *Solar Cells* 2 (2) (1980) 151–166. doi:10.1016/0379-6787(80)90007-1. URL <http://linkinghub.elsevier.com/retrieve/pii/S0379678780900071>
- [2] A. Cuevas, A. Luque, J. Eguren, J. del Alamo, [50 Per cent more output power from an albedo-collecting flat panel using bifacial solar cells](#), *Solar Energy* 29 (5) (1982) 419–420. doi:10.1016/0038-092X(82)90078-0. URL <http://www.sciencedirect.com/science/article/pii/S0038092X82900780>
- [3] R. Guerrero-Lemus, R. Vega, T. Kim, A. Kimm, L. E. Shephard, [Bifacial solar photovoltaics A technology review](#), *Renewable and Sustainable Energy Reviews* 60 (2016) 1533–1549. doi:10.1016/j.rser.2016.03.041. URL <http://www.sciencedirect.com/science/article/pii/S1364032116002768>
- [4] A. Luque, E. Lorenzo, G. Sala, S. Lpez-Romero, [Diffusing reflectors for bifacial photovoltaic panels](#), *Solar Cells* 13 (3) (1985) 277–292. doi:10.1016/0379-6787(85)90021-3. URL <http://linkinghub.elsevier.com/retrieve/pii/S0379678785900213>
- [5] Y. K. Chieng, M. A. Green, [Computer simulation of enhanced output from bifacial photovoltaic modules](#), *Progress in Photovoltaics: Research and Applications* 1 (4) (1993) 293–299. doi:10.1002/pip.4670010406. URL <http://onlinelibrary.wiley.com/doi/10.1002/pip.4670010406/abstract>
- [6] U. Yusufoglu, T. Pletzer, L. Koduvelikulathu, C. Comparotto, R. Kopecek, H. Kurz, [Analysis of the Annual Performance of Bifacial Modules and Optimization Methods](#), *IEEE Journal of Photovoltaics* 5 (1) (2015) 320–328. doi:10.1109/JPHOTOV.2014.2364406.
- [7] J. Appelbaum, [View Factors to Grounds of Photovoltaic Collectors](#), *Journal of Solar Energy Engineering* 138 (6) (2016) 064501–064501–6. doi:10.1115/1.4034316. URL <http://dx.doi.org/10.1115/1.4034316>
- [8] G. J. Janssen, B. B. Van Aken, A. J. Carr, A. A. Mewe, [Outdoor Performance of Bifacial Modules by Measurements and Modelling](#), *Energy Procedia* 77 (2015) 364–373. doi:10.1016/j.egypro.2015.07.051. URL <http://linkinghub.elsevier.com/retrieve/pii/S187661021500819X>
- [9] J. E. Castillo-Aguilella, P. S. Hauser, [Multi-Variable Bifacial Photovoltaic Module Test Results and Best-Fit Annual Bifacial Energy Yield Model](#), *IEEE Access* 4 (2016) 498–506. doi:10.1109/ACCESS.2016.2518399.
- [10] M. Lave, J. S. Stein, L. Burnham, [Performance Results for the Prism Solar Installation at the New Mexico Regional Test Center: Field Data from February 15 - August 15, 2016](#), Tech. Rep. SAND2016-9253, Sandia National Laboratories., Albuquerque, NM (2016). URL <http://energy.sandia.gov/download/38750/>
- [11] S. Guo, T. M. Walsh, M. Peters, [Vertically mounted bifacial photovoltaic modules: A global analysis](#), *Energy* 61 (2013) 447–454. doi:10.1016/j.energy.2013.08.040. URL <http://www.sciencedirect.com/science/article/pii/S0360544213007275>
- [12] J. Appelbaum, [Bifacial photovoltaic panels field](#), *Renewable Energy* 85 (2016) 338–343. doi:10.1016/j.renene.2015.06.050. URL <http://www.sciencedirect.com/science/article/pii/S0960148115300732>
- [13] [International Technology Roadmap for Photovoltaic Results 2015, Seventh edition](#), Tech. rep., ITRPV (Oct. 2016). URL [/Reports/Downloads/2016/](#)
- [14] D. Passias, B. Kllbck, [Shading effects in rows of solar cell panels](#), *Solar Cells* 11 (3) (1984) 281–291. doi:10.1016/0379-6787(84)90017-6. URL <http://www.sciencedirect.com/science/article/pii/S0379678784900176>
- [15] J. Bany, J. Appelbaum, [The effect of shading on the design of a field of solar collectors](#), *Solar Cells* 20 (3) (1987) 201–228. doi:10.1016/0379-6787(87)90029-9. URL <http://www.sciencedirect.com/science/article/pii/S0379678787900299>
- [16] K. Doubleday, B. Choi, D. Maksimovic, C. Deline, C. Olalla, [Recovery of inter-row shading losses using differential power-processing submodule DCDC converters](#), *Solar Energy* 135 (2016) 512–517. doi:10.1016/j.solener.2016.06.013. URL <http://www.sciencedirect.com/science/article/pii/S0038092X1630192X>
- [17] N. Y. Fathi, A. Samer, [View Factors of Flat Solar Collectors Array in Flat, Inclined, and Step-Like Solar Fields](#), *Journal of Solar Energy Engineering* 138 (6) (2016) 061005–061005–8. doi:10.1115/1.4034549. URL <http://dx.doi.org/10.1115/1.4034549>
- [18] C. R. Snchez Reinoso, D. H. Milone, R. H. Buitrago, [Simulation of photovoltaic centrals with dynamic shading](#), *Applied Energy* 103 (2013) 278–289. doi:10.1016/j.apenergy.2012.09.040. URL <http://www.sciencedirect.com/science/article/pii/S0306261912006812>
- [19] M. J. Adinoyi, S. A. M. Said, [Effect of dust accumulation on the power outputs of solar photovoltaic modules](#), *Renewable Energy* 60 (2013) 633–636. doi:10.1016/j.renene.2013.06.014. URL <http://www.sciencedirect.com/science/article/pii/S0960148113003078>
- [20] N. Bouaouadja, S. Bouzid, M. Hamidouche, C. Bousbaa, M. Madjoubi, [Effects of sandblasting on the efficiencies of solar panels](#), *Applied Energy* 65 (1) (2000) 99–105. doi:10.1016/S0306-2619(99)00044-6. URL <http://www.sciencedirect.com/science/article/pii/S0306261999000446>
- [21] H. Lu, L. Lu, Y. Wang, [Numerical investigation of dust pollution on a solar photovoltaic \(PV\) system mounted on an isolated building](#), *Applied Energy* 180 (2016) 27–36. doi:10.1016/j.apenergy.2016.07.030. URL <http://www.sciencedirect.com/science/article/pii/S0306261916309722>
- [22] K. Menoufi, [Dust Accumulation on the Surface of Photovoltaic Panels: Introducing the Photovoltaic Soiling Index \(PVSI\)](#), *Sustainability* 9 (6) (2017) 963. doi:10.3390/su9060963. URL <http://www.mdpi.com/2071-1050/9/6/963>
- [23] S. A. Janko, M. R. Arnold, N. G. Johnson, [Implications of high-penetration renewables for ratepayers and utilities in the residential solar photovoltaic \(PV\) market](#), *Applied Energy* 180 (2016) 37–51. doi:10.1016/j.apenergy.2016.07.041. URL <http://www.sciencedirect.com/science/article/pii/S0306261916309825>
- [24] C. S. Lai, M. D. McCulloch, [Levelized cost of electricity for solar photovoltaic and electrical energy storage](#), *Applied Energy* 190 (2017) 191–203. doi:10.1016/j.apenergy.2016.12.153. URL <http://www.sciencedirect.com/science/article/pii/S030626191631933X>
- [25] I. Reda, A. Andreas, [Solar position algorithm for solar radiation applications](#), *Solar Energy* 76 (5) (2004) 577–589. doi:10.1016/j.solener.2003.12.003.

- URL <http://www.sciencedirect.com/science/article/pii/S0038092X0300450X>
- [26] PV Performance Modeling Collaborative | An Industry and National Laboratory collaborative to improve Photovoltaic Performance Modeling (2016).
URL <https://pvpmc.sandia.gov/>
- [27] B. Haurwitz, *Insolation in relation to cloudiness and cloud density*, *Journal of Meteorology* 2 (3) (1945) 154–166. doi:10.1175/1520-0469(1945)002<0154:IIRTCA>2.0.CO;2.
URL [http://journals.ametsoc.org/doi/abs/10.1175/1520-0469\(1945\)002<0154:IIRTCA>2.0.CO;2](http://journals.ametsoc.org/doi/abs/10.1175/1520-0469(1945)002<0154:IIRTCA>2.0.CO;2)
- [28] B. Haurwitz, *Insolation in relation to cloud type*, *Journal of Meteorology* 3 (4) (1946) 123–124. doi:10.1175/1520-0469(1946)003<0123:IIRTCT>2.0.CO;2.
URL [http://journals.ametsoc.org/doi/abs/10.1175/1520-0469\(1946\)003<0123:IIRTCT>2.0.CO;2](http://journals.ametsoc.org/doi/abs/10.1175/1520-0469(1946)003<0123:IIRTCT>2.0.CO;2)
- [29] POWER, *Surface meteorology and Solar Energy: A renewable energy resource web site (release 6.0)* (2017).
URL <https://eosweb.larc.nasa.gov/cgi-bin/sse/sse.cgi?>
- [30] J. F. Orgill, K. G. T. Hollands, *Correlation equation for hourly diffuse radiation on a horizontal surface*, *Solar Energy* 19 (4) (1977) 357–359. doi:10.1016/0038-092X(77)90006-8.
URL <http://www.sciencedirect.com/science/article/pii/0038092X77900068>
- [31] J. A. Duffie, W. A. Beckman, *Solar Engineering of Thermal Processes: Duffie/Solar Engineering 4e*, John Wiley & Sons, Inc., Hoboken, NJ, USA, 2013.
URL <http://doi.wiley.com/10.1002/9781118671603>
- [32] E. L. Maxwell, *A Quasi-Physical Model for Converting Hourly Global Horizontal to Direct Normal Insolation*, Tech. Rep. SERI/TR-215-3087, Solar Energy Research Inst., Golden, CO (USA) (Aug. 1987).
URL <https://www.osti.gov/scitech/biblio/5987868>
- [33] D. G. Erbs, S. A. Klein, J. A. Duffie, *Estimation of the diffuse radiation fraction for hourly, daily and monthly-average global radiation*, *Solar Energy* 28 (4) (1982) 293–302. doi:10.1016/0038-092X(82)90302-4.
URL <http://www.sciencedirect.com/science/article/pii/0038092X82903024>
- [34] D. T. Reindl, W. A. Beckman, J. A. Duffie, *Diffuse fraction correlations*, *Solar Energy* 45 (1) (1990) 1–7. doi:10.1016/0038-092X(90)90060-P.
URL <http://www.sciencedirect.com/science/article/pii/0038092X9090060P>
- [35] L. T. Wong, W. K. Chow, *Solar radiation model*, *Applied Energy* 69 (3) (2001) 191–224. doi:10.1016/S0306-2619(01)00012-5.
URL <https://www.sciencedirect.com/science/article/pii/S0306261901000125>
- [36] P. G. Loutzenhiser, H. Manz, C. Felsmann, P. A. Strachan, T. Frank, G. M. Maxwell, *Empirical validation of models to compute solar irradiance on inclined surfaces for building energy simulation*, *Solar Energy* 81 (2) (2007) 254–267. doi:10.1016/j.solener.2006.03.009.
URL <http://www.sciencedirect.com/science/article/pii/S0038092X06000879>
- [37] R. R. Perez, P. Ineichen, R. D. Seal, E. L. Maxwell, A. Zelenka, *Dynamic global-to-direct irradiance conversion models*, *ASHRAE Transactions* 98 (1) (1992) 354–369.
URL <https://archive-ouverte.unige.ch/unige:38583>
- [38] N. Martn, J. M. Ruiz, *Annual angular reflection losses in PV modules*, *Progress in Photovoltaics: Research and Applications* 13 (1) (2005) 75–84. doi:10.1002/pip.585.
URL <http://onlinelibrary.wiley.com/doi/10.1002/pip.585/abstract>
- [39] Keith R. McIntosh, Simeon C. Baker-Finch, *Tracey* (Nov. 2013).
URL <https://www2.pvlighthouse.com.au/Simulation/Hosted/Tracey/Tracey.aspx>
- [40] K. R. McIntosh, J. N. Cotsell, J. S. Cumpston, A. W. Norris, N. E. Powell, B. M. Ketola, *An optical comparison of silicone and EVA encapsulants for conventional silicon PV modules: A ray-tracing study*, in: 2009 34th IEEE Photovoltaic Specialists Conference (PVSC), 2009, pp. 000544–000549. doi:10.1109/PVSC.2009.5411624.
- [41] K. R. McIntosh, J. N. Cotsell, A. W. Norris, N. E. Powell, B. M. Ketola, *An optical comparison of silicone and EVA encapsulants under various spectra*, in: 2010 35th IEEE Photovoltaic Specialists Conference, 2010, pp. 000269–000274. doi:10.1109/PVSC.2010.5615830.
- [42] C. Deline, A. Dobos, S. Janzou, J. Meydbray, M. Donovan, *A simplified model of uniform shading in large photovoltaic arrays*, *Solar Energy* 96 (2013) 274–282. doi:10.1016/j.solener.2013.07.008.
URL <http://www.sciencedirect.com/science/article/pii/S0038092X13002739>
- [43] M. F. Modest, *Radiative heat transfer*, third edition Edition, Academic Press, New York, 2013, oCLC: ocn813855549.
URL <http://www.sciencedirect.com/science/book/9780123869449>
- [44] *Calculating the additional energy yield of bifacial solar modules*, White paper, SolarWorld (2016).
URL <https://www.solarworld-usa.com/~media/www/files/white-papers/calculating-additional-energy-yield-through-bifacial-solar-tech.pdf?la=en>
- [45] A. Luque, S. Hegedus (Eds.), *Handbook of Photovoltaic Science and Engineering*, Second Edition, 2011.
URL <http://onlinelibrary.wiley.com/book/10.1002/9780470974704>
- [46] A. Lindsay, M. Chiodetti, P. Dupeyrat, D. Binesti, E. Lutun, K. Radouane, *Key Elements in the Design of Bifacial PV Power Plants*, 31st European Photovoltaic Solar Energy Conference and Exhibition (2015) 1764–1769doi:10.4229/EUPVSEC20152015-5C0.14.4.
URL <http://www.eupvsec-proceedings.com/proceedings?paper=33705>
- [47] H. K. Hajjar, F. A. Dubaikel, I. M. Ballard, *Bifacial photovoltaic technology for the oil and gas industry*, in: 2015 Saudi Arabia Smart Grid (SASG), 2015, pp. 1–4. doi:10.1109/SASG.2015.7449283.

Supplementary Information: Vertical Bifacial Solar Farms: Physics, Design, and Global Optimization

M. Ryyan Khan ^{b,1}, Amir Hanna ^{a,1}, Xingshu Sun ^{b,1}, Muhammad A. Alam ^{b,1,*}

^aElectrical Engineering Department, King Abdullah University of Science and Technology, Saudi Arabia
^bSchool of Electrical and Computer Engineering, Purdue University, West Lafayette, IN 47906, United States

arXiv:1704.08630v2 [physics.app-ph] 29 Nov 2017

S1. Panel efficiency under uniform illumination

The efficiency η_{diff} of the panel under isotropic illumination can be estimated from the weighted average of $\eta(\theta)$ over all the solid angles. However, we calculate η and η_{diff} for a realistic panel using the simulator ‘Tracey’ [1, 2, 3]. The simulator does ray tracing for a panel structure considering interface reflections, scattering from metal fingers, and losses in glass and encapsulation. We assume modules that have square cells (15.6 cm). There is 3 busbars per cell, where the busbar width is 0.15 cm and the bus finger pitch is 0.2 cm. The bus finger thickness is 150 μm . The thicknesses of the encapsulation (EVA) and glass layers are 450 μm and 0.2 cm, respectively. For simplicity, the edge losses are neglected in the efficiency calculation.

We simulate two specific cases: (i) direct light incident normal to the panel, (ii) isotropic (diffused) light incident on the panel. We assume illumination on a single face of the panel. The ray tracer finds light absorption and combines the result with a typical internal quantum efficiency (IQE) of a Si-panel to find short circuit current. We assume open circuit voltage of 0.68V, and 78.5% fill factor (FF)—this yielded in $\eta = 18.9\%$ and $\eta_{diff} = 15.67\%$ under normal and diffused illumination on a single face of the panel.

S2. Panel operation under partial shading

S2.1. Panel configuration

The panel is composed of series connected cells. The full configuration is assumed to be divided into N_{bypass} rows of sub-strings, see Fig. S1(a). Each sub-string is protected by a bypass-diode. For the calculation reported in this paper, we assume $N_{bypass} = 3$ as shown in Fig. S1(b). With a panel height of h , each sub-string section has a height of $h_N = h/N_{bypass}$.

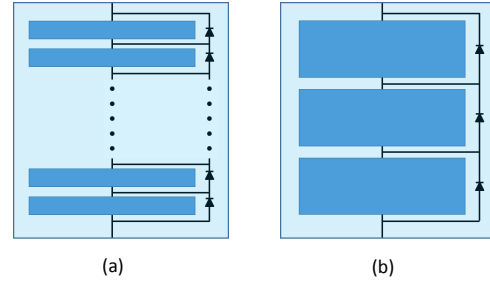


Figure S1: (a) A schematic configuration of the panel. Each sub-string (blue block) consists of several series connected cells (not shown separately), and has a bypass-diode in parallel. There are N_{bypass} sub-strings in series. (b) A specific case when $N_{bypass} = 3$.

S2.2. Non-uniform illumination

Partial shading creates non-uniform illumination across the panel, with the bottom receiving less energy compared to the top. The statement is obvious for the direct light. As discussed in the main manuscript, shadow height on the bottom of the panel is h_s —this height will change throughout the day as the position of the sun changes, indicating that the lower part of the panel receives less energy than the top.

The considerations are slightly more complicated for diffuse and albedo light. Similar to the direct light, the diffuse insolation provides higher intensity towards the top-edge of the panel compared to the bottom-edge due to partial shading between panels. On the other hand, the scattered albedo provides higher intensity close to ground (bottom-edge) compared to the top-edge of the panel. Despite this counter-acting intensity profiles of diffuse and albedo lights, our calculations show that for ground reflectance of 0.3-0.6 and for all practical p/h and clearness indices, the combined illumination from diffuse and albedo light yields in a profile with the lowest intensity towards the bottom of the panel.

S2.3. Panel output calculation steps

We utilize the analytical model developed in Ref. [4] to find how the panel configured with 3-bypass diodes

*Corresponding author

Email address: alam@purdue.edu (Muhammad A. Alam)

¹The authors contributed equally.

respond to non-uniform illumination. The model assumes diffuse light (diffuse insolation and albedo combined) $\widehat{I}_{PV(d,A)}^{(bifacial)}$ uniformly illuminating the panel. This is also the lower limit to the panel output when the panel is mostly shadowed. However, as we have explained in the preceding section, the bottom section of the panel has the lowest contribution from the combined diffuse insolation and albedo. We can thus define this lower output limit from the diffused light collection at the bottom section of the panel:

$$\widehat{I}_{PV(d,A)}^{(bifacial)} = \frac{1}{h_N} \int_0^{h_N} \left(\widehat{I}_{PV(diff)}^{(bifacial)}(z) + \widehat{I}_{PV(Alb)}^{(bifacial)}(z) \right) dz \quad (S1)$$

Next, the output from direct light assuming unshaded panels (mutual shading neglected) is as follows:

$$\widehat{I}_{PV(dir),UnSh}^{(bifacial)} = \frac{1}{h} \int_0^h \widehat{I}_{PV(dir)}^{(bifacial)}(z) dz \quad (S2)$$

The ‘diffused fraction’ is therefore,

$$f_D = \frac{\widehat{I}_{PV(d,A)}^{(bifacial)}}{\widehat{I}_{PV(d,A)}^{(bifacial)} + \widehat{I}_{PV(dir),UnSh}^{(bifacial)}} \quad (S3)$$

Finally, the overall power reduction f_{out} is found as a function of $(N_{bypass}, h_s/h, f_D, FF)$ (see Equ. (15) in Ref. [4]). The output is then:

$$\widehat{I}_{PV}^{(bifacial)} = f_{out} \times \left(\widehat{I}_{PV(d,A)}^{(bifacial)} + \widehat{I}_{PV(dir),UnSh}^{(bifacial)} \right), \quad (S4)$$

$$I_{PV}^{(bifacial)} = \frac{h}{p} \widehat{I}_{PV}^{(bifacial)}. \quad (S5)$$

Here, $\widehat{I}_{PV}^{(bifacial)}$ and $I_{PV}^{(bifacial)}$ are total output *per panel area* and *per farm area*, respectively.

S3. Global output with array period

As discussed in the main manuscript, instead of optimizing for the period p of the vertical panel array, we may need to fix p for maintenance purposes. For example, Fig. S2 shows yearly yield of the farm for set $p = 1, 2, 3m$. The optimum p/h is within 0.8-1.1m (we have $h = 1.2m$); therefore for larger periods (e.g., $p = 2, 3m$), the output will be lower, as seen in Fig. S2.

S4. Illustrative discussion on specific locations

In this section, we will discuss insolation and farm yield for five specific locations listed in Table S1. The regions span across continents, have very different elevation and cloudiness (characterized by clearness index). Our goal is to illustrate the validity of the model by focusing on energy output in specific regions of the world. The GHI and location specific elevation are found from NASA Surface

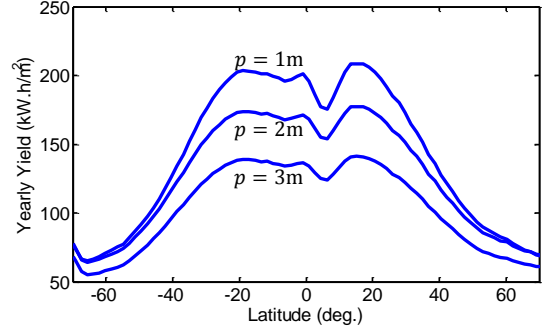


Figure S2: Yearly yield (averaged over longitudes) of the vertical bifacial farm as function of latitude for set periods of $p = 1, 2, 3m$.

Table S1: List of location for the illustrative discussion. The elevation values of the corresponding locations are found from the NASA-database. The yearly average clearness index is found based on the insolation model described in the main text.

	(Lat., Long.)	Elevation	Avg. yearly \bar{k}_T
Washington DC	38.9N, 77.04W	85m	0.4853
Leadville, Colorado	39.25N, 106.29W	2653m	0.5751
Broken Hill, Australia	32S, 141.5E	253m	0.6147
Kamuthi, India	9.35N, 78.39E	64m	0.5341
Schipkau, Germany	51.57N, 13.98E	71m	0.4209

meteorology and Solar Energy database [5]. The average yearly clearness index (or annual clearness index), \bar{k}_T is found from GHI and extraterrestrial insolation of the respective locations.

The monthly insolation of GHI extracted from the NASA-database for each of the locations are shown by blue symbols in Fig. S3. As explained in the main text, the GHI is then split into DHI and DNI based on elevation of the respective locations. Australia being in the Southern hemisphere, has lowest GHI in June (winter), as expected. These insolation information are then used to calculate farm output. Monthly yield of bifacial (red circles) and monofacial (cyan triangles) farms assuming 2m row-spacing are shown in Fig. S3 for each of the locations. The monofacial panels are, of course, optimally tilted as a function of latitude (tilt = $0.69 \times |\text{Lat}| + 3.7^\circ$) [6]. For this row-spacing, vertical bifacial solar farm yields higher compared to monofacial farms.

The integrated yearly GHI for the locations under current study are shown in Fig. S4. Here, Broken Hill, Australia show the highest yearly GHI and highest \bar{k}_T . Both these values are the lowest for Schipkau, Germany. The corresponding yearly yields of the vertical and monofacial farms are also shown in Fig. S4. For the 2m row-spacing farm design, the vertical bifacial farms yield more compared to monofacial farms, as discussed in the main text.

Finally, the yearly yield for period-optimized farms (by maximizing output) are shown in Fig. S5. The bifacial farm optimizes at $p/h \sim 1$. The monofacial farm optimizes

at $p/h \sim 1.1$ to 1.3 for the selected locations. This translates into very small row spacing ($< 0.5\text{m}$) for $h = 1.2\text{m}$, as explained in the main manuscript. However, these results in Fig. S5 indicates the maximum possible yield from vertical bifacial and monofacial farms for these locations.

References

- [1] Keith R. McIntosh, Simeon C. Baker-Finch, Tracey (Nov. 2013). URL <https://www2.pvlighthouse.com.au/Simulation/Hosted/Tracey/Tracey.aspx>
- [2] K. R. McIntosh, J. N. Cotsell, J. S. Cumpston, A. W. Norris, N. E. Powell, B. M. Ketola, An optical comparison of silicone and EVA encapsulants for conventional silicon PV modules: A ray-tracing study, in: 2009 34th IEEE Photovoltaic Specialists Conference (PVSC), 2009, pp. 000544–000549. doi: 10.1109/PVSC.2009.5411624.
- [3] K. R. McIntosh, J. N. Cotsell, A. W. Norris, N. E. Powell, B. M. Ketola, An optical comparison of silicone and EVA encapsulants under various spectra, in: 2010 35th IEEE Photovoltaic Specialists Conference, 2010, pp. 000269–000274. doi: 10.1109/PVSC.2010.5615830.
- [4] C. Deline, A. Dobos, S. Janzou, J. Meydbray, M. Donovan, A simplified model of uniform shading in large photovoltaic arrays, Solar Energy 96 (2013) 274–282. doi:10.1016/j.solener.2013.07.008. URL <http://www.sciencedirect.com/science/article/pii/S0038092X13002739>
- [5] POWER, Surface meteorology and Solar Energy: A renewable energy resource web site (release 6.0) (2017). URL <https://eosweb.larc.nasa.gov/cgi-bin/sse/sse.cgi?>
- [6] A. Luque, S. Hegedus (Eds.), Handbook of Photovoltaic Science and Engineering, Second Edition, 2011. URL <http://onlinelibrary.wiley.com/book/10.1002/9780470974704>

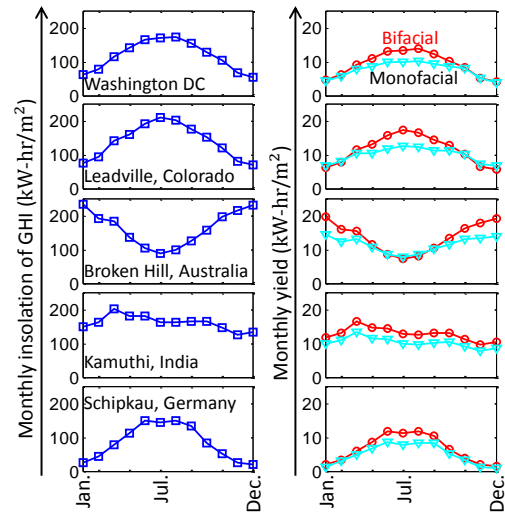


Figure S3: Monthly GHI extracted from NASA-database are shown by blue squares. Assuming 2m row-spacing, calculated monthly output from vertical bifacial (red circles) and monofacial (cyan triangles) farms are also shown.

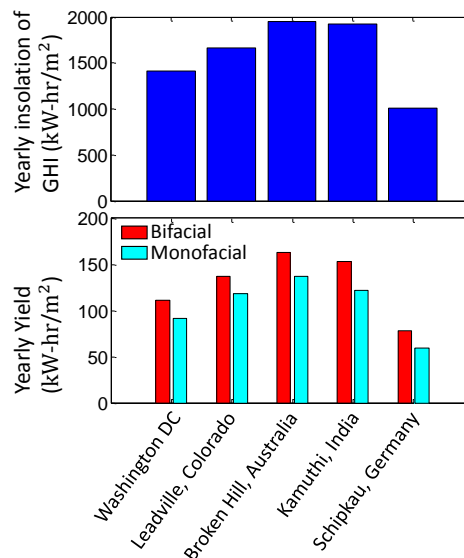


Figure S4: Integrated yearly GHI, and the farm output (2m row-spacing) are shown for the locations listed in Table S1.

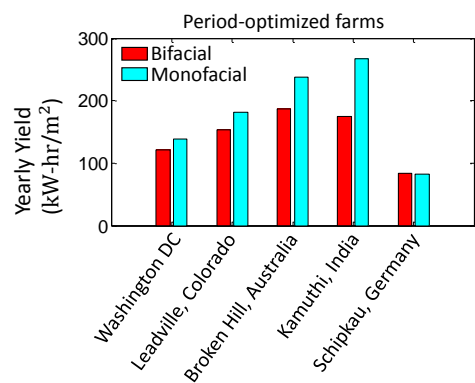


Figure S5: Integrated yearly farm output (period optimized for maximum yield) are shown for the locations listed in Table S1.